Journal of Nuclear Materials 518 (2019) 95–107

Contents lists available at ScienceDirect

Journal of Nuclear Materials

journal homepage: www.elsevier.com/locate/jnucmat

Local chemical instabilities in 20Cr–25Ni Nb-stabilised austenitic stainless steel induced by proton irradiation

C. Barcellini [a, *], R.W. Harrison [b], S. Dumbill [c], S.E. Donnelly [b], E. Jimenez-Melero [a]

[a] Materials Performance Centre, School of Materials, The University of Manchester, Manchester, M13 9PL, United Kingdom
[b] School of Computing and Engineering, University of Huddersfield, Huddersfield, HD1 3DH, United Kingdom
[c] National Nuclear Laboratory, Sellafield, Seascale, CA20 1PG, United Kingdom

HIGHLIGHTS

- Proton-irradiated AGR cladding develops solute redistribution at defect sinks.
- The elemental profile shape depends on grain boundary character and temperature.
- Few boundaries have a local Cr content ≤12 wt% and profile widths ≥100 nm.
- HAGB with misorientation ≥40° become mobile at ≥460 °C and show asymmetric profiles.
- Si and Ni segregation at carbide interface hints to a transition towards G-phase.

GRAPHICAL ABSTRACT

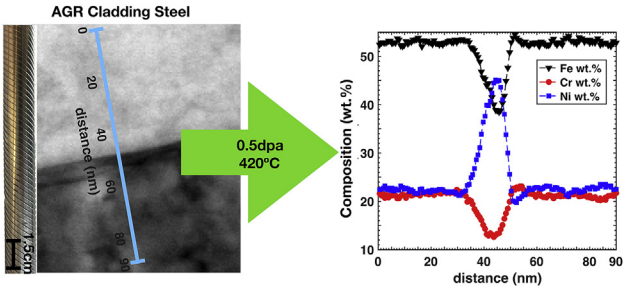

ARTICLE INFO

Article history:
Received 26 November 2018
Received in revised form
20 February 2019
Accepted 21 February 2019
Available online 25 February 2019

Keywords:
Austenitic stainless steel
Proton irradiation
Radiation-induced segregation
Transmission electron microscopy
Advanced gas-cooled reactors

ABSTRACT

We have assessed the local solute redistribution at defect sinks in 20Cr–25Ni Nb-stabilised austenitic stainless steel after proton irradiation at three temperatures, i.e. 420, 460 and 500 °C, up to a maximum damage level of 0.8 dpa. This material is currently being used as cladding in Advanced Gas-cooled Reactors (AGR), and potential local Cr depletions would compromise its resistance to intergranular corrosion attack during wet storage of spent fuel elements. Irradiation induces the depletion of Cr, Fe and, to a lesser extent, Mn from grain boundaries, whereas Ni and Si become enriched at those locations. The elemental profiles are symmetric and primarily W-shaped at 420 °C, whereas at higher temperatures asymmetric and double-peaked profiles are also detected, most likely as a result of grain boundary migration. High-angle grain boundaries with a misorientation angle ≥40° become mobile at 460 °C and especially at 500 °C, and also experience a relatively large solute redistribution, with local Cr contents in a significant number of boundaries falling below 12 wt% and profile widths ≥100 nm. However, coincidence site lattice boundaries (CSL) Σ3 boundaries prove to be resistant to Cr depletion and to boundary mobility. Local elemental patterns at radiation-induced dislocations seem to mimic those at grain boundaries, but do not trigger the formation of Ni_3Si precipitates. Additionally, Ni and Si form a shell-like structure around the pre-existing Nb(C,N) precipitates, potentially leading to the transition into G-phase at higher damage levels.

* Corresponding author.University of Manchester, School of Materials, Materials Performance Centre, Oxford Road, Manchester, M13 9PL, United Kingdom.
E-mail address: chiara.barcellini@postgrad.manchester.ac.uk (C. Barcellini).

https://doi.org/10.1016/j.jnucmat.2019.02.035
0022-3115/

1. Introduction

The fuel cladding material currently used in Advanced Gas-cooled Reactors (AGRs) is a Nb-stabilised austenitic stainless steel grade, containing 20 wt%Cr, 25 wt%Ni and ≥0.7 wt% Nb [1]. A stabilisation heat treatment is performed to the cladding at 930 °C for ~1 h prior to its lifetime in the reactor core, in order to precipitate a fine dispersion of Nb(C,N) particles in the austenitic matrix [2]. Those fine precipitates help to control the austenite grain size at elevated temperatures [2], increase the cladding resistance to thermal creep in the oxidising AGR core environment [3], and also hinder the formation of Cr carbo-nitrites and consequently the local Cr depletion at the grain boundaries of the austenitic matrix [4]. However, despite the formation of Nb(C,N) particles during cladding processing, the high-temperature environment of the AGR core, coupled with intense neutron fluxes and the CO_2-1-2%CO coolant, can induce a detrimental reduction in Cr content at grain boundaries and other preferential lattice sites. Once the nuclear fuel is discharged, it is planned to be stored together with its cladding material in caustic-dosed water ponds for at least 25 years [5], before its permanent storage in a future geological disposal facility. Potential local reductions in Cr content would decrease the cladding resistance to intergranular corrosion attacks (IGCAs) during its temporary storage in water-based environments. Since the Windscale Inquiry in 1977, it is deemed possible that 20Cr–25Ni Nb-stabilised stainless steel may experience an increased susceptibility to IGCAs after neutron irradiation [6], a phenomenon termed Radiation-Induced Sensitisation (RIS).

The current understanding relates RIS phenomenon to the redistribution of solute atoms in the vicinity of grain boundaries and other lattice sites, due to the coupling of solute fluxes with the diffusion of radiation-induced vacancies and self-interstitials towards defect sinks present in the microstructure [7]. In other nuclear-grade austenitic steels, this process results in the Cr depletion at grain boundaries, concomitantly with the local enrichment in Ni and potentially also in Si [8–11]. In the case of AGR steel cladding, RIS is expected to affect only those fuel pins that either operate in a temperature range of 350–530 °C, or spend a significant amount of time in that temperature window during removal from the reactor core, with a peak effect at ~420 °C [12,13]. Recent reports indicate that the variability in chemical profiles measured in irradiated nuclear steels is at least partially related to the specific boundary geometry [14–17]. In this respect, special grain boundaries such as the coincidence lattice site Σ3, seem to be particularly resistant to local Cr depletion due to their relatively high symmetry. In contrast, non-special high-angle grain boundaries are the most affected by Cr depletion [15,17]. Additionally, alternative defect sinks such second phase particles or dislocation structures show affinity for radiation-induced vacancies, and therefore reduce the magnitude of the RIS effect at grain boundaries [9]. Furthermore, radiation-induced and -enhanced second phases have been observed in 20Cr–25Ni Nb-stabilised stainless steel, neutron irradiated at selected damage levels and local reactor temperatures [18,19].

A systematic study of the RIS phenomenon in irradiated steel claddings is fundamental for the future medium-to-long-term wet storage of AGR fuel elements. In this study, we have characterised the chemical redistributions induced by proton bombardment in the microstructure of 20Cr–25Ni Nb-stabilised stainless steel. The proton irradiation experiment at three selected temperatures, i.e. 420 °C, 460 °C and 500 °C, was performed in a transmission electron microscope (TEM) coupled to an ion accelerator [20,21], in order to monitor in-situ the early stages of radiation damage. The occurrence and evolution of dislocation structures, voids and stacking fault tetrahedra as the damage level increases up to 0.8 dpa are described in a companion paper [22]. Here we report the local changes in elemental composition at grain boundaries and other lattice defects or interfaces present in the steel microstructure, observed at the aforementioned temperatures and at the highest damage levels of 0.5 and 0.8 dpa. In the past, intense proton beams have been used successfully to simulate the neutron damage in other nuclear steel grades with minimal sample activation [11,23,24]. However, most RIS reports in the literature relate to austenitic stainless steels used as internals in Light Water Reactors, whose core temperatures are significantly lower than those in AGRs. Systematic information regarding RIS in AGR steels is a prerequisite to link the atomic-scale changes at the grain boundaries and other preferential sites in the structure with potential localised corrosion attacks during wet storage of spent fuel elements.

2. Experimental

The chemical composition of the AGR cladding steel used in this study is reported in Table 1. The as-received material was in the form of a 55 cm-long tube with transverse ribs on the outer surface for better heat transfer to the CO_2-1-2%CO gas coolant. The tube had an outer diameter of 1.5 cm and an average wall thickness of 0.4 cm. After the removal of the external ribs, we extracted samples with a size of $2.5 \times 2.5\ cm^2$ and subjected them to a recrystallisation annealing at 930 °C for 40 min in inert atmosphere, followed by water quenching down to room temperature. The heat-treated samples were mechanically ground and polished with a colloidal silica suspension with a 0.25 μm grain size. The structural characterisation of the as-recrystallised material was performed using a FEI Quanta 650 scanning electron microscope equipped with an electron backscattered diffraction (EBSD) detector. The EBSD data processing was performed using the MTEX software [27]. The grain boundaries were classified into low-angle grain boundaries (LAGB) presenting a misorientation angle between 2° and 15° [26,27], coincidence site lattice sites (CSL) [28,29] and high-angle grain boundaries (HAGB). A high-angle grain boundary was classified as a CSL boundary of the type Σ3, Σ5, Σ9 or Σ11 when the Brandon's criterion was satisfied [30]. Other types of CSL boundaries were not considered in this study, since they were not observed in significant numbers. The length fraction was calculated as the ratio between the length of a certain type of boundary and the total length of grain boundaries observed in the EBSD map of a given sample. Furthermore, 3 mm-diameter TEM discs were extracted from the as-recrystallised material and electro-polished at a temperature of −25 °C, using an electrolyte consisting of 95 vol% methanol −5 vol% perchloric acid (60%). Three equivalent TEM disks, with a thickness in the range of 110–140 nm, as derived from convergent beam electron diffraction patterns (CBED) [31], were irradiated with a 40 keV proton beam at the three selected temperatures of 420, 460 and 500 °C. A fourth disc was used as a reference, in order to assess the lattice defect structures induced by proton bombardment.

The proton irradiations were performed at the Microscope and

Table 1
Chemical composition (wt%) of 20Cr–25Ni stainless steel grade used in this study.

C	Mn	Si	S	P	Cu	Ni	Cr	Mo	Nb	V	Al	Ti	N	Fe
0.058	0.59	0.58	0.002	<0.003	<0.01	23.98	19.12	<0.01	0.57	<0.01	0.017	0.01	0.009	Bal.

Ion Accelerator for Materials Investigation - 2 system (MIAMI-2 system), located at the University of Huddersfield, UK. The samples were mounted sequentially on a high-temperature double-tilt holder and placed inside a 300 kV Hitachi H-9500 TEM, equipped with a LaB_6 electron source (with a spatial resolution of 0.14 nm) and a Gatan OneView digital camera with 16 megapixels and up to 300 fps video. The TEM is installed at the end of a beam line connected to an ion accelerator. The proton beam enters the microscope chamber at 18.7° with respect to the electron beam. We used a proton beam energy of 40 keV. The Bragg peak position would be at ~200 nm from the sample surface exposed to the incoming proton beam, based on SRIM simulations [32], therefore beyond the sample thickness determined by CBED. We performed three irradiation experiments at the selected temperatures of 420 °C, 460 °C and 500 °C, and at a proton flux of $\sim 8 \cdot 10^{13}$ $ions/cm^2 s$, corresponding to a dose rate of $\sim 2 \cdot 10^{-4}$ dpa/s.

Afterwards, the chemical changes induced by proton irradiation were characterised ex-situ using a FEI Talos F200A TEM/STEM microscope. The electron source is an FEI X-FEG high brightness source able to deliver $1.8 \cdot 10^9\ A \cdot cm^{-2} \cdot sr^{-1}$ at an accelerating voltage of 200 kV. This microscope is equipped with a FEI Ceta 16 M camera with an acquisition rate of 25 fps, a high angle annular dark field detector (HAADF) with a resolution of 0.16 nm, and a bright and dark field detector. This microscope also has a FEI Super-X integrated EDS system, composed of four windowless silicon drift detectors (SDDs) with a mapping capability up to 10^5 spectra/s. They are symmetrically placed around the electron beam in order to maximise the collection angle [33]. Each 2-D chemical map was acquired for 30 min using a 700 pA electron beam current. The length of the boundary segments analysed within those maps varied between 150 nm and 800 nm. The data were acquired at zero tilt angle, in order to maximise the signal on the SDDs, and only those grain boundaries whose plane was normal to the incident electron beam were considered for analysis. The elemental quantification based on the acquired spectra was performed using the FEI Velox software after background subtraction. The elemental composition as a function of the distance with respect to the grain boundary was obtained by integrating along straight segments (1-D elemental profiles) for 100 pixels. The error related to the quantification of each single element was calculated considering the Gaussian peak profile of the collected EDX spectra. Thus, the estimated error at 99.7% confidence, based on the total number of counts for each peak used in the elemental quantification was ~1% for Fe, ~1.5% for Ni and Cr, ~3.1% for Si, ~3.2% for Mn and ~1% for Nb (reduced to ~0.5% for particles). For each boundary, five 1-D profiles, collected at neighbouring positions along the grain boundary

Table 2
Grain boundary elemental composition and width of the elemental profile (d) as a function of the grain boundary misorientation angle for the three temperatures investigated.

420 °C, 0.5dpa												
θ(°)	Cr (wt.%)	σ(wt.%)	Ni (wt.%)	σ(wt.%)	Fe (wt.%)	σ(wt.%)	Si (wt.%)	σ(wt.%)	Mn (wt.%)	σ(wt.%)	d (nm)	σ(nm)
27.2	19.1	0.2	29.4	0.4	48.0	0.4	1.2	0.1	1.5	0.1	31.9	5.9
31.2	13.0	0.7	48.7	2.4	36.2	1.7	1.6	0.1	1.3	0.3	21.1	1.5
31.3	14.5	0.2	35.7	1.4	45.4	0.6	2.8	0.02	1.1	0.1	14.6	1.4
31.6	14.9	0.2	33.8	1.1	32.4	0.5	2.8	0.2	1.0	0.1	15.3	0.6
36.1	18.6	0.3	30.6	0.4	46.8	0.5	1.6	0.2	1.5	0.1	13.3	
38.7	17.5	0.3	28.6	0.4	48.7	2.1	1.7	0.1	1.3	0.3	24.6	1.6
39.1	17.8	1.3	29.9	2.1	48.4	0.9	1.7	0.2	1.1	0.1	32.7	7.5
41.0	20.3	0.2	23.9	0.6	52.1	0.6	1.3	0.1	1.5	0.02	0.0	0
46.2	15.6	0.9	34.9	0.5	45.5	0.5	1.6	0.1	1.3	0.2	20.3	2.6
59.6	18.5	0.2	30.6	0.6	47.3	0.4	1.4	0.1	0.0	–	47.6	9.3
60	20.8	–	23.2	–	53.4	–	1.22	–	1.48	–	0	–
460°C, 0.8dpa												
12.3	17.4	0.3	31.6	0.4	47.8	0.4	1.4	0.1	1.1	0.05	25.1	3
26.3	12.8	2.6	43.6	6.7	40.4	4	1.1	0.06	1.2	0.2	77.1	23.5
44.1	13.9	0.4	43.9	1.3	38.6	0.8	1.5	0.1	1.0	0.04	53.0	2.5
44.6	19.0	0.3	27.9	0.8	49.9	0.1	1.2	0.1	1.3	0.1	129.5	4.5
44.6	18.3	0.5	30.7	2.8	47.9	1.8	1.3	0.3	1.4	0.1	92.2	1.6
45.8	17.4	–	31.6	–	47.8	–	1.1	–	1.4	–	124.5	–
50.1	11.6	0.4	49.3	1.1	36.4	0.9	1.1	0.1	1.0	0.1	111.0	8.2
50.2	12.6	–	46.4	–	38.3	–	1.2	–	1.0	–	117.9	–
55.8	15.3	–	39.7	–	42.1	–	1.0	–	1.2	–	144.5	–
56.7	14.2	0	41.2	1.4	41.4	1.8	0.9	0.2	1.2	0.04	83.0	1.4
56.7	11.1	0	35.5	0.8	50.6	0.8	1.1	0.04	1.0	0.3	122.5	9.2
57.4	8.8	0.6	58.9	0.3	27.3	0.4	1.2	0.04	0.9	0.04	83.8	5
58.1	9.0	0.5	54.2	0.6	34.0	5	1.2	0.02	1.0	0.03	93.8	1.5
58.7	9.6	–	52.8	–	34.8	–	1.2	–	1.0	–	82.7	–
60.0	19.2	–	24.8	–	51.5	–	1.5	–	1.6	–	0.0	–
500°C, 0.8dpa												
25.6	7.5	1.2	61.2	0.9	23.5	1.4	4.3	0.4	1.0	0.1	149.9	53.2
28.0	12.6	1.2	57.2	2.9	24.1	1.9	3.9	0.1	1.0	0.1	35.1	3.2
30.7	14.6	0.7	53.0	1.0	25.7	2.5	4.4	0.1	1.2	0.1	20.4	1.3
31.0	14.2	1.1	54.7	1.6	25.9	1.3	3.9	0.2	1.2	0.2	21.1	2.9
33.6	6.5	1.3	49.4	1.5	40.5	0.7	2.2	0.4	0.8	0.1	243.7	9.8
39.4	7.8	2.4	55.3	4.7	32.6	3.0	1.8	0.1	0.8	0.2	108.5	44.7
40.5	11.0	2.7	47.1	9.0	37.3	7.1	2.4	0.2	1.0	0.1	102.3	25.3
43.8	14.3	0.2	36.8	3.2	43.4	1.9	2.1	0.1	0.8	0.04	40.4	10.2
47.9	7.0	1.8	59.8	3.9	26.8	1.4	3.1	0.2	0.8	0.2	202.8	20.2
58.7	8.2	1.5	55.8	3.5	30.6	2.2	3.4	0.5	0.9	0.1	277.8	40.2
59.6	8.3	1.1	54.5	2.1	31.9	1.2	2.9	0.2	0.8	0.04	229	40.8
60.0	21.3	–	20.0	–	52.6	–	1.8	–	2.9	–	0.0	–

line, were averaged in order to obtain the elemental compositional profile [34]. The elemental concentration corresponding to the average of the peak values over those five profiles for a given grain boundary is reported in Table 2, together with the standard deviation.

The misorientation angle of the studied grain boundaries was determined by Transmission Kikuchi Diffraction (TKD) [35,36], using an FEI Magellan HR FEG-SEM equipped with an electron backscattered diffraction detector (EBSD). The TKD data were acquired using an accelerating voltage of 20 kV, a beam current of 0.8 nA and a step size of 0.08 μm, with the sample tilted 20° with respect to the EBSD detector. The TKD data processing was performed using the MTEX software [25]. For each boundary we measured between 2 and 8 points and the misorientation angles reported in Table 2 are the average between these measures.

3. Results

The resultant steel microstructure after the 40 min heat treatment at 930 °C is shown in Fig. 1. The recrystallised microstructure is characterised by an average austenite grain diameter of ~10 μm and smooth recrystallised grains, see illustrative examples in Fig. 1a–c. Moreover, we observed a bimodal Nb(C,N) size distribution: a limited number of relatively large particles, often surrounded by a network of dislocation lines (Fig. 1d), together with a fine dispersion of particles heterogeneously distributed in the austenitic matrix, see Fig. 1e and f. This fine dispersion is composed of both intergranular and intragranular particles, often observed in the form of particle clusters, whose spatial distribution is a reminiscence of the dislocation lines present in the microstructure prior to recrystallisation, see Fig. 1e. An EBSD map with the grain boundaries coloured according to their misorientation angle (θ) is shown in Fig. 1g. The heat treatment at 930 °C generates a relatively high number of annealing twin boundaries (CSL Σ3), i.e. ~45% of the total grain boundary length, together with ~36% of HAGBs and only ~19% of low-angle grain boundaries.

The detailed characterisation of the lattice defect evolution as a function of damage level up to 0.8 dpa is presented in a companion paper [22]. In the present study, we report the local changes of chemical composition at the highest damage level of this experiment, namely 0.5 dpa at 420 °C, and 0.8 dpa at both 460 °C and 500 °C. STEM BF micrographs of the final proton-induced damaged microstructure are displayed in Fig. 2 for the three irradiation temperatures. At those three temperatures, $\frac{a_0}{3}\langle 111\rangle$ Frank partials and perfect $\frac{a_0}{2}\langle 110\rangle$ dislocation loops are present in the microstructure. A higher irradiation temperature implies a larger average

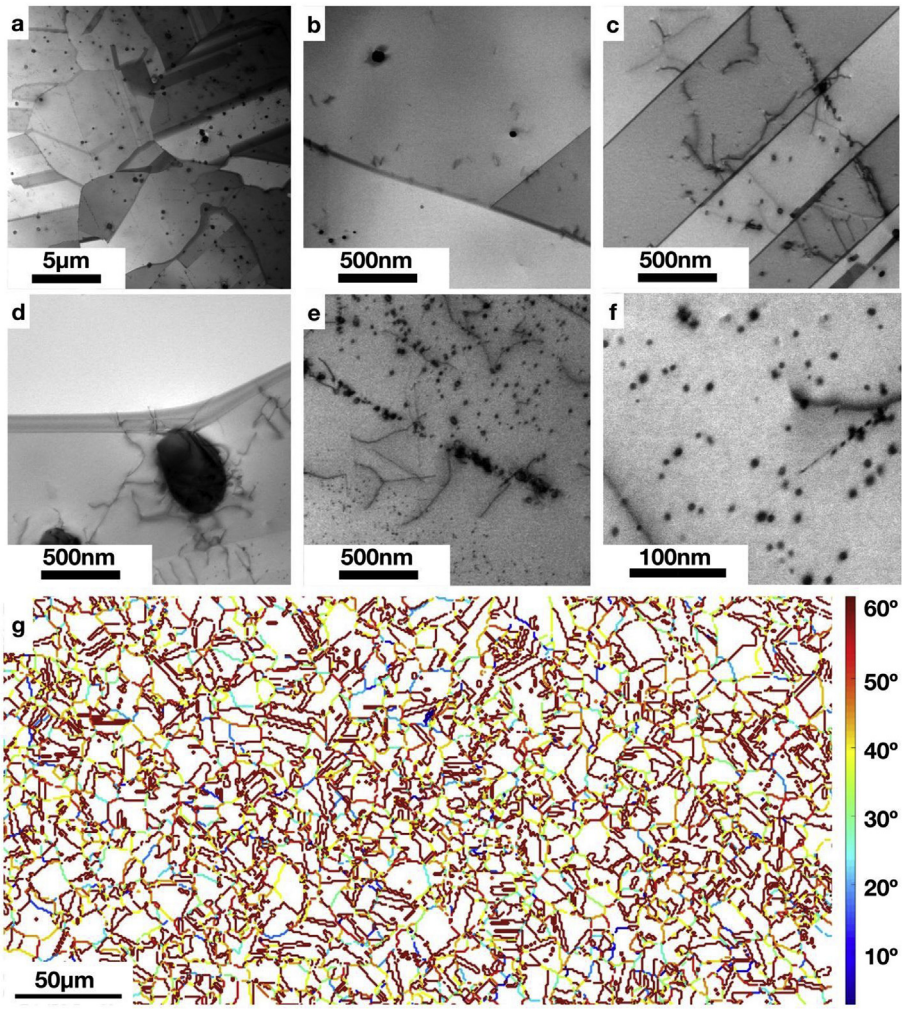

Fig. 1. BF STEM micrographs of (a) recrystallised austenite grains, (b) a grain boundary, (c) twin boundaries with precipitates and dislocations, (d) a residual Nb(C,N) at a grain boundary surrounded by a network of dislocations, (e) a fine dispersion of Nb(C,N) precipitated along a dislocation line and intergranularly, (f) a fine detail of the smaller Nb(C,N) particles observed in the recrystallised grains, and (g) an EBSD colour map where the grain boundaries have been coloured according to their misorientation angle.

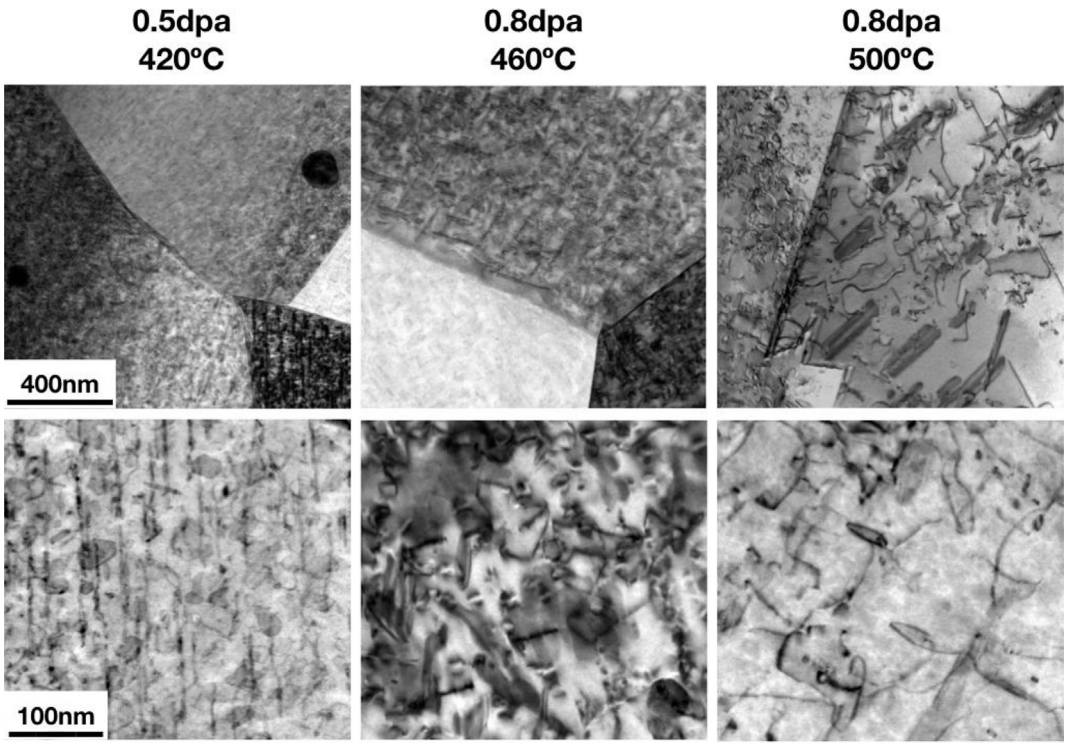

Fig. 2. STEM BF micrographs of the radiation-induced damaged microstructure at the three irradiation temperatures investigated.

size and lower density of dislocation loops. Those perfect loops evolve into dislocation lines that form a dense network at the damage level of 0.8 dpa (460 °C) and already at 0.2 dpa (500 °C), respectively [22]. Voids were also detected at 460 °C and 500 °C, whereas stacking fault tetrahedra (SFT) were observed at 0.8 dpa only for the highest temperature of 500 °C.

Local chemical redistributions were detected at grain boundaries (Fig. 3), dislocations (Fig. 4) and particle/matrix interfaces (Fig. 5) at the three irradiation temperatures. For all those types of defect sinks, we observed the depletion of Cr, Fe and to a lower extent of Mn, together with local enrichment of Ni and Si. Fig. 3 contains examples of chemical profiles collected across grain boundaries, whereas a summary of the chemical composition of all the grain boundaries checked in this study, together with the boundary misorientation angle and the thickness of the elemental profile, is presented in Table 2. The value reported for the chemical composition are the peak values of each single boundary profile, averaged over five profiles as explained in the experimental session. The magnitude of Cr depletion increases with damage level and irradiation temperature. At the three irradiation temperatures, the CSL Σ3 boundaries are found to be resistant to radiation-induced chemical redistribution, see Fig. 3.

At 420 °C the grain boundary with the largest Cr depletion was a HAGB with $\theta = 31.2°$, presenting a local Cr content as low as 13 wt% and a profile width of ~21 nm, whereas the widest profile (i.e. 47.6 nm) was observed for a higher misorientation of $\theta = 59.6°$. At this irradiation temperature, the width of the elemental profile decreases with increasing magnitude of Cr depletion. The relative change in Cr content is −9.4 wt% on average, and we did not observe any grain boundary with a Cr content ≤12 wt%. The profile shape presents primarily a W-shape for Cr and Mn, without any significant asymmetry. Furthermore, Cr depletion also occurred close to dislocations, coupled with the first signs of Ni and Si segregation and clustering. In the first row of Fig. 4 a few clusters of Ni and Si can be observed in the elemental maps, whereas an example of chemical profile obtained by integrating along a dislocation line (outlined with a red square in the BF STEM image of Fig. 4) is shown. The maximum elemental variation observed at dislocations was ~−7% (Cr), ~+9% (Ni), ~+39% (Si) and ~−11% (Mn), respectively. Both Nb(C,N) populations did not present signs of chemical segregation at this irradiation temperature and damage level, as revealed by the data presented in Fig. 5 for the sample irradiated at 420 °C and the one in the as-recrystallised state as reference.

In contrast with the highly-symmetric W-shaped profiles observed at 420 °C, a variety of elemental profile shapes was observed at the higher temperature of 460 °C: symmetric, asymmetric and double-peak profiles. The symmetric elemental profiles correspond to grain boundaries with relatively low misorientation angles, i.e. $\theta<30°$, whereas all boundaries with higher misorientation angles present either asymmetric or double-peak profiles. Selected examples of elemental profiles at 460 °C are shown in the middle column of Fig. 3. Asymmetric profiles may be an indication that the boundary has moved during the irradiation experiment, potentially 'dragging' the elemental profiles during grain boundary migration. A clear evidence of this phenomenon can be observed in Fig. 6, where a representative grain boundary is shown at different damage levels. The chemical analysis of this boundary reveals that the Si profile remains symmetric and narrower than the Cr and Ni profiles (Fig. 7), remaining centred close to the original position of the grain boundary.

At 460 °C, the width of the elemental profile also decreases with increasing magnitude of Cr depletion. It is worth noting that the 33% of the studied grain boundaries at 460 °C present a Cr content lower than 12 wt% at 0.8 dpa and those highly depleted in Cr correspond to HAGBs with a misorientation angle $\theta>50°$. Furthermore, the elemental redistribution at dislocations increases in magnitude and profile thickness, with a maximum relative variation of −11% (Cr), +19% (Ni), +51% (Si), −21% (Mn), respectively. Additionally, a characteristic shell-like structure is formed around a

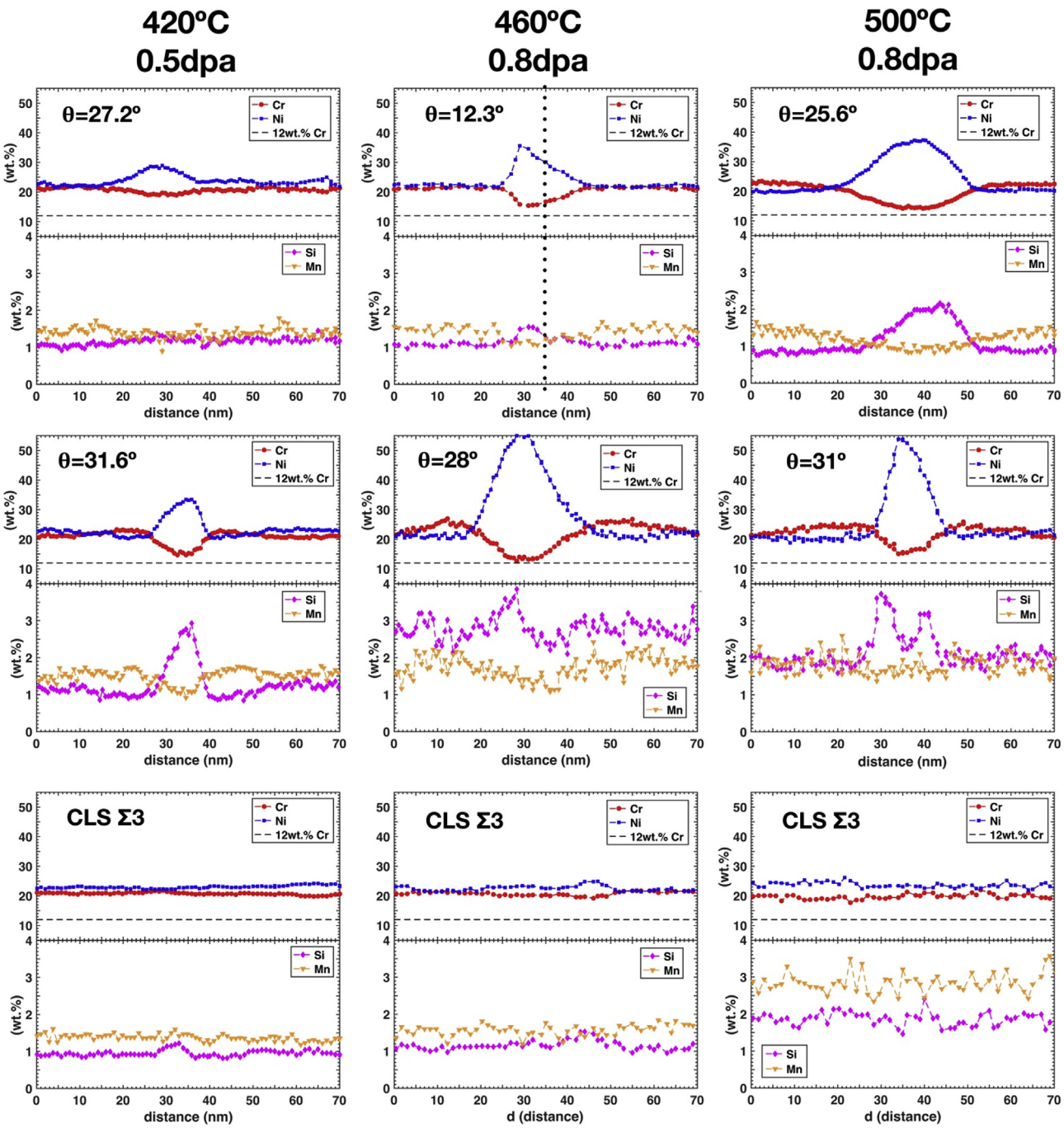

Fig. 3. Grain boundary elemental profiles for the three irradiation temperatures investigated, showing illustrative examples of the profile shape and magnitude with the misorientation angle of the grain boundary.

number of Nb(C,N) particles, with Ni and Si both segregating at the particle/matrix interface, see Fig. 5.

At the highest temperature of 500 °C, the magnitude of the elemental depletion/segregation is more pronounced than at lower temperatures, see Fig. 3. Moreover, in some cases the width of the Cr depletion profiles attains values close to 200 nm, see Fig. 7, and a significant number of grain boundaries present a Cr content below 12 wt%. If the maximum in the Si profile depicts the original position of the grain boundary, the width of the Cr profile can be taken as the migration distance of the grain boundary. The migrating boundaries are all HAGBs with a misorientation angle ranging from 30° to 59°. Furthermore, the elemental redistribution at dislocations and particle/matrix interfaces also increases in intensity and width as compared to 460 °C. Clear signs of Si and Ni segregation and clustering can be observed in the elemental maps of Fig. 4, together with segregation at dislocations lines (the profile is obtained integrating along the dislocation line in the red square in the STEM BF image). The Ni and Si segregation surrounding pre-existing Nb(C,N) particles is more intense than at lower temperatures, see Fig. 5b.

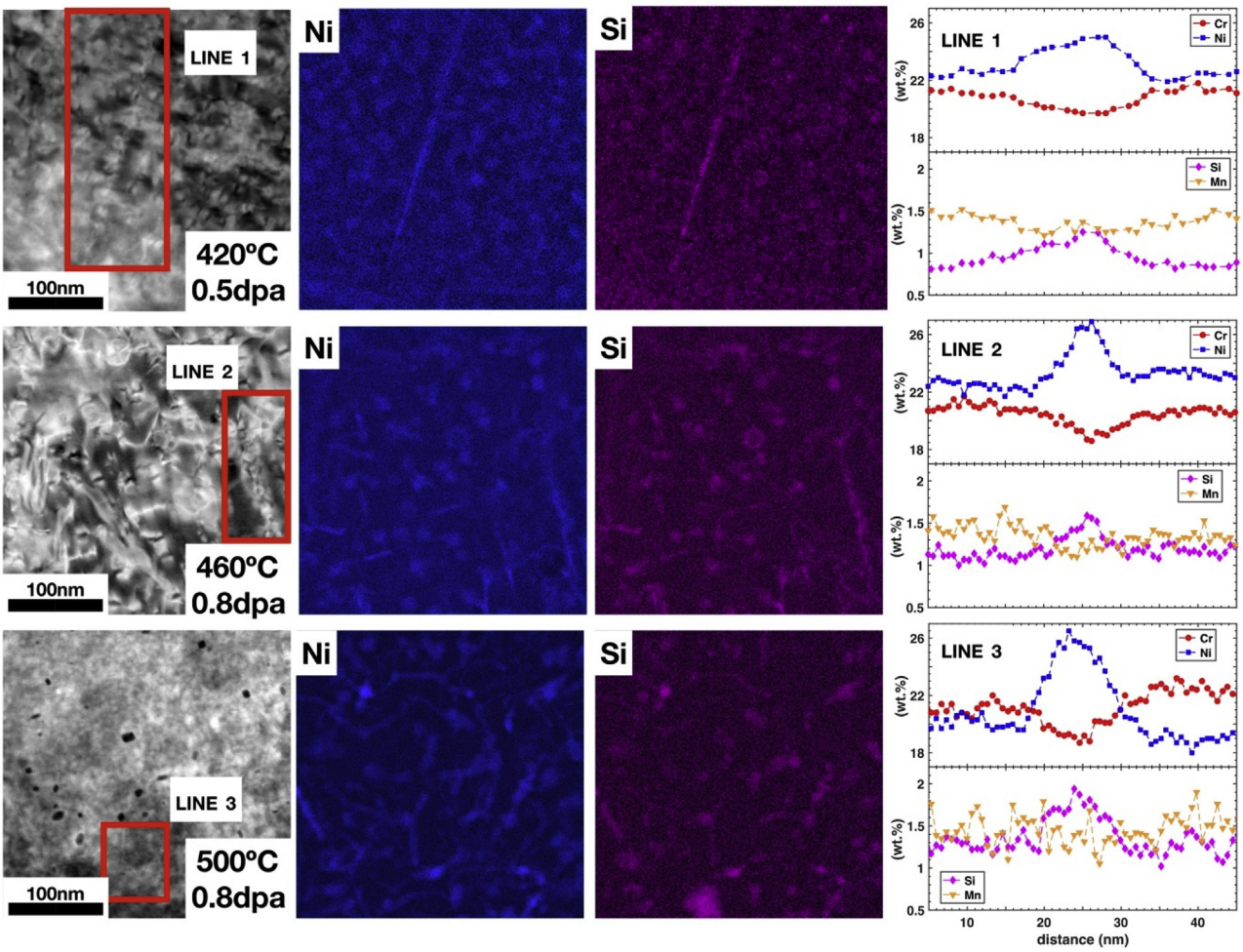

Fig. 4. STEM BF micrographs revealing dislocation structures induced by proton irradiation for the three irradiation temperatures investigated (left column), together with corresponding EDS Ni and Si maps (middle rows) and elemental profiles (right column) of the area outlined by the red square in the left column. (For interpretation of the references to colour in this figure legend, the reader is referred to the Web version of this article.)

4. Discussion

After proton irradiation, elemental segregation or depletion has been detected at grain boundaries at the three irradiation temperatures, namely 420 °C, 460 °C and 500 °C. In the analysed boundaries, Cr, Fe and to a lesser extent Mn become depleted, whereas the Ni and Si content increases with respect to their concentration in the matrix. On the other hand, Nb remains bound in the Nb(C,N) particles present already in the as-recrystallised microstructure. The resultant elemental profiles are generally interpreted as a consequence of the inverse Kirkendall effect, i.e. the generation of a balancing flux of atoms in the presence of a flux of radiation-induced point defects [37]. RIS modelling in binary [38] and ternary Fe-based alloys [39], considering mainly a vacancy-based mechanism, reveals that the sign of the ratio between the concentration gradient for a certain element and the concentration gradient for vacancies determines the direction of RIS, i.e. depletion or segregation at grain boundaries [7]. If this ratio is positive, the solute element moves in the same direction of the vacancy flux, i.e. towards grain boundaries, therefore it segregates at those boundaries, otherwise it depletes. The sign for Cr and Ni in austenitic steels are negative and positive respectively, therefore Cr depletes and Ni segregates at grain boundaries [40], in accordance to our experimental results.

The intensity and width of the elemental profile increases with temperature, and at 500 °C a Cr content as low as 6.5 wt% was measured for a limited number of grain boundaries. The temperature dependence of RIS for neutron-irradiated AGR cladding stainless steel was modelled for a dose rate typical of the AGR reactor core ($2 \cdot 10^{-8}$ dpa/s) and a damage level of 1 dpa [41]. The model predicts the RIS phenomenon to take place in the range from 350 °C to 530 °C, with a peak effect at 420 °C [42]. At higher irradiation temperatures, radiation-induced solute redistribution would be mitigated by enhanced point defect recombination, due to an increased number of thermally-produced point defects and back diffusion of alloying elements driven by the solute concentration gradient [43]. The difference between the dose rate used in the present study, i.e. $2 \cdot 10^{-4}$ dpa/s, and that used in the model to simulate neutron-induced RIS, would take into account for the shift in the temperature at which the maximum effect is observed [42,43].

For a given irradiation temperature, there is a significant variation in the magnitude of the elemental depletion/segregation from boundary to boundary. Fig. 8 shows the dependence of the elemental content at grain boundaries with the misorientation angle. The Cr depletion is negligible when the misorientation angle of the CSL Σ3 boundary (60°) is approached. This experimental observation is consistent with those reported for other proton-

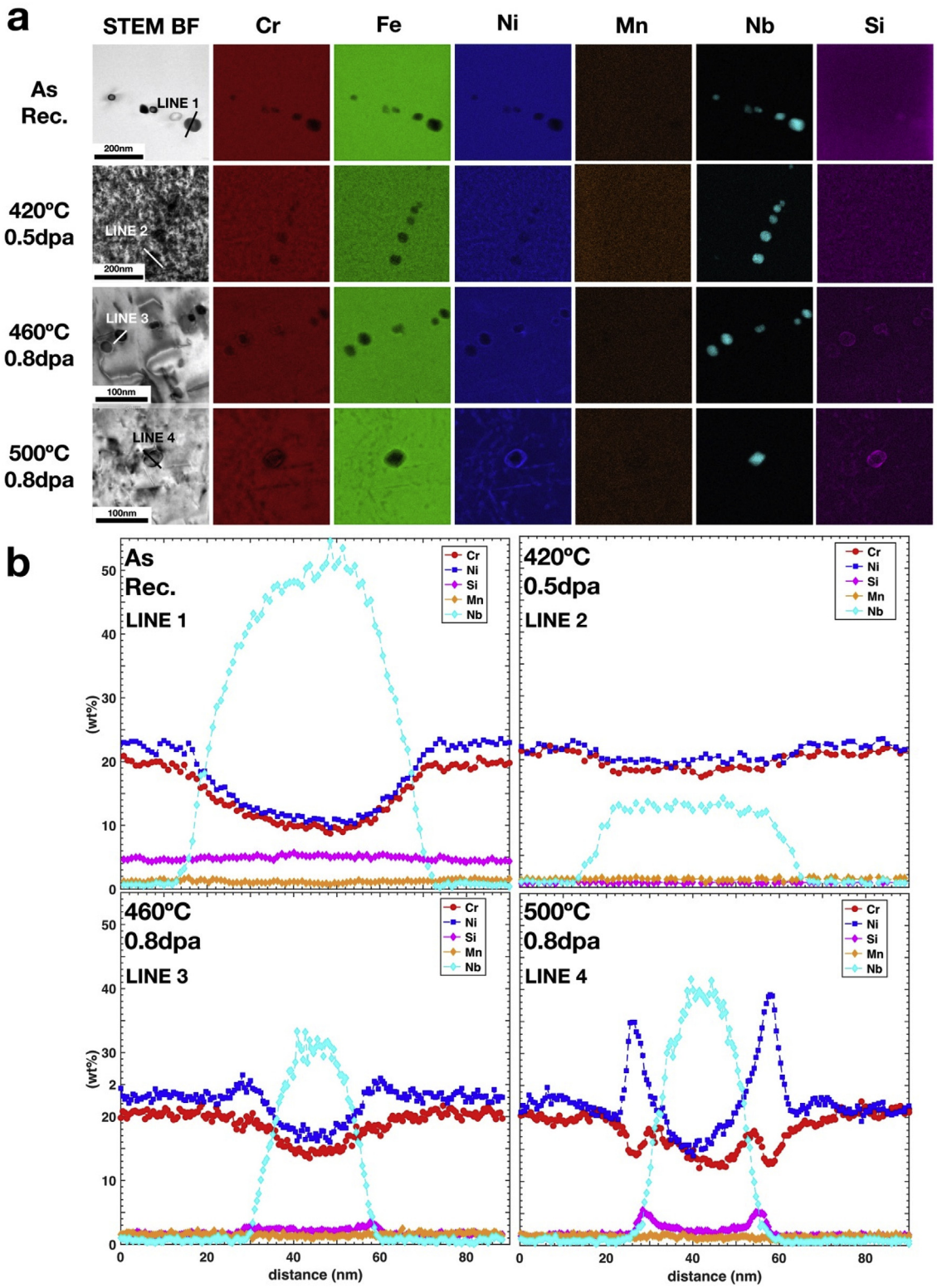

Fig. 5. (a) STEM BF micrographs and EDS elemental maps in an area containing Nb(C,N) particles. The colour intensity in each EDS is proportional to the amount (in wt.%) of the specific element measured. (b) Examples of 1-D elemental profiles in the vicinity and through Nb(C,N) particles.

irradiated [14–17] and thermally-sensitised steel grades [44–47]. In those previous studies, twin boundaries were found to be resistant to local solute redistributions. The resistance to local Cr depletion is related to the intrinsic boundary structure, which underpins its energy. Our results reveal a cuspid in the local Cr content when the misorientation angle approaches 60°, see Fig. 8. The lack of Cr depletion can be attributed to the high coherence across the CSL Σ3 boundaries, which are not perfect sinks due to the fact that there are no fast diffusion paths within the boundary for point defects to diffuse and annihilate [15,17]. Since the annihilation rate

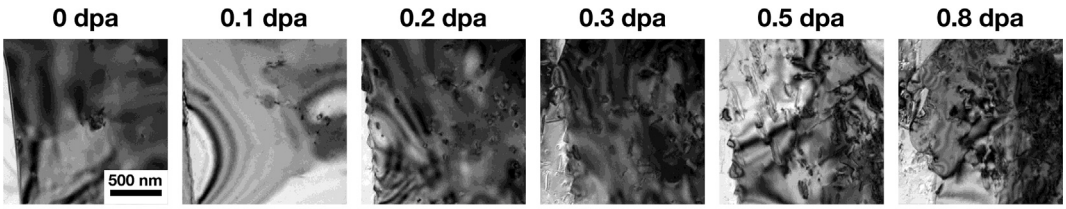

Fig. 6. TEM BF micrographs acquired with the electron beam parallel to [$\bar{1}$11] direction showing the migration of a HAGB during in-situ proton irradiation at 500 °C [24].

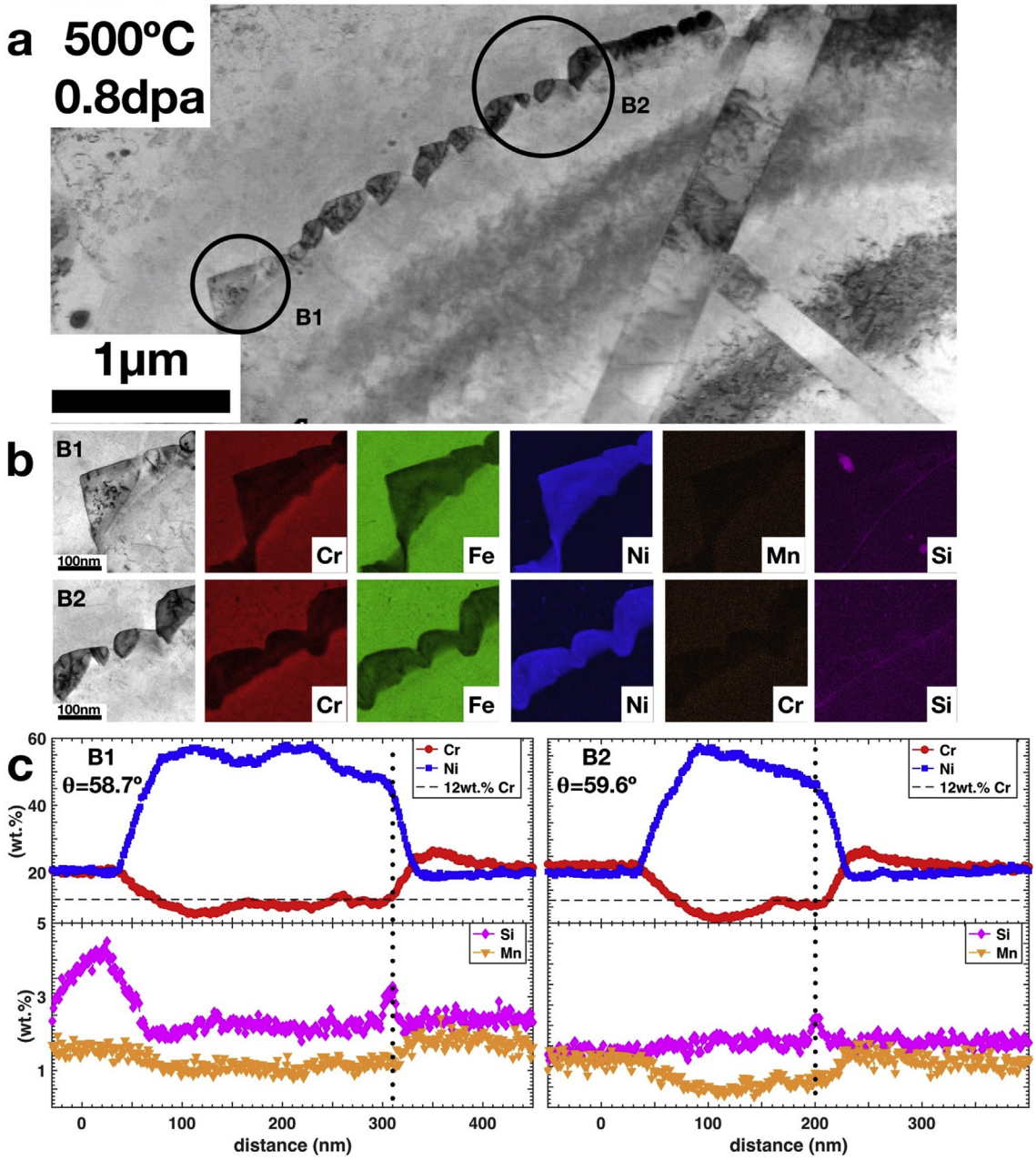

Fig. 7. (a) STEM BF micrographs of a migrating boundary at 500 °C and 0.8 dpa. (b) STEM BF micrographs and EDS maps of two representative regions of the moving boundary in (a). (c) Grain boundary elemental profiles of the boundary regions shown in (b).

for point defects is low at CSL Σ3 boundaries, the local point defect concentration would be higher than thermal equilibrium, resulting in reduced fluxes of vacancies and interstitials towards those special grain boundaries. An opposite situation is found instead for HAGBs, which behave as perfect sinks with a relatively high rate of defect annihilation. HAGBs are composed of a high density of

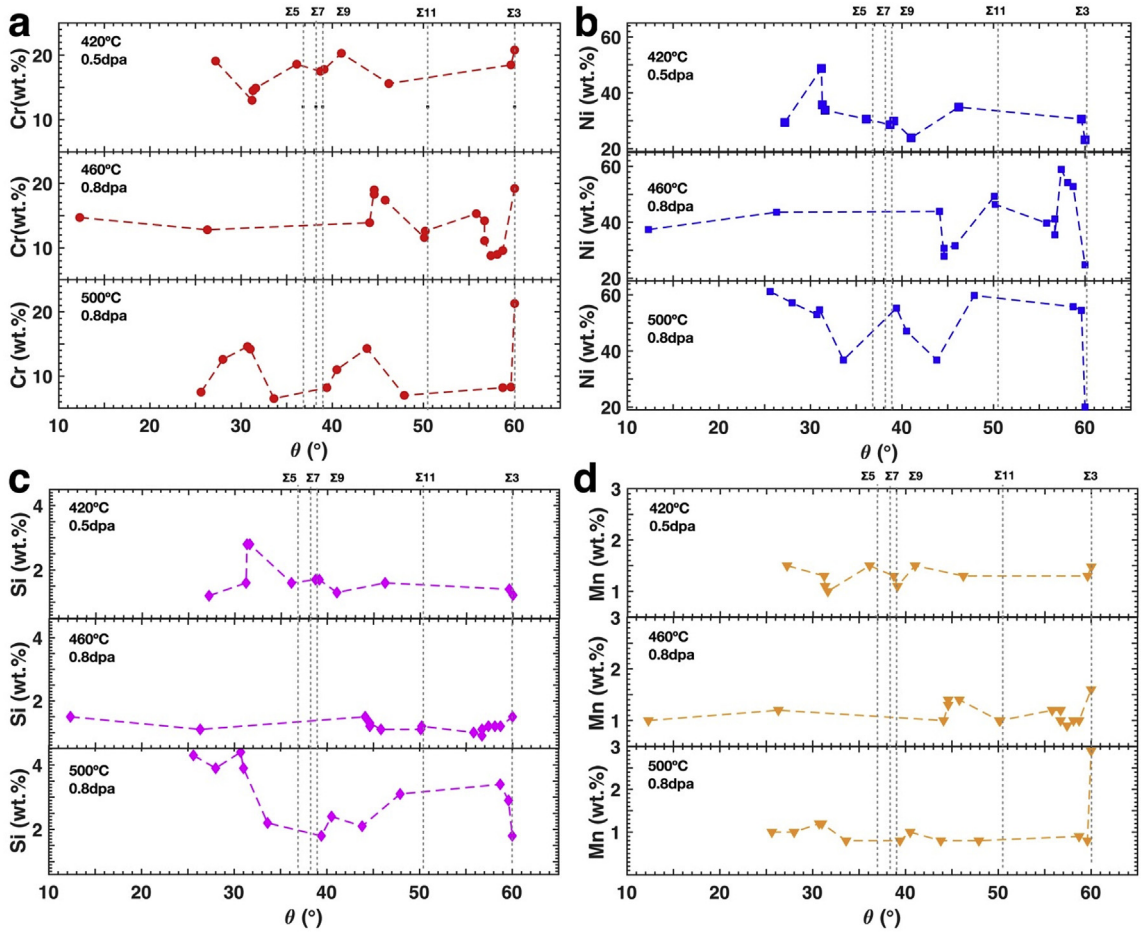

Fig. 8. Variation of (a) Cr, (b) Ni, (c) Si and (d) Mn content at grain boundaries as a function of the misorientation angle for the three irradiation temperatures investigated. The grey vertical lines indicate the position of special CLS boundary Σ3, Σ5, Σ9 and Σ11.

dislocations which act as annihilation sites for point lattice defects. The relatively low point defect concentration at HAGBs induces enhanced defect fluxes and, as a consequence, a larger Cr depletion or Ni & Si segregation at those HAGBs.

In addition, a variety of profile shapes was measured at 460 °C and 500 °C, including double peaked and asymmetric profiles extending in some cases for ≥100 nm, whereas at 420 °C only symmetric and relatively narrow elemental profiles were detected. The high density of radiation-induced dislocations inside the neighbouring grains competes with the grain boundaries for the diffusing point defects, therefore reducing the flux of point defects towards grain boundaries. At 420 °C we have not detected any significant grain boundary migration, whereas at 460 °C a limited number of grain boundaries start migrating, and this phenomenon becomes more pronounced at 500 °C, see Fig. 7. The observed elemental profile starts to develop at the original boundary position, but as the boundary moves, the solute atoms start to deplete/segregate at the new position of the boundary at a given moment in time. The migrating boundary wipes up a significant fraction of the radiation-induced dislocations. Therefore, the elemental profile related to the new boundary position has not only less time to develop, but it is also affected on the side ahead of the migrating boundary by the higher content of matrix dislocations than the back side of the boundary [13]. As can be clearly observed in Fig. 7, grain boundaries 'drag' with them the profile of all solute elements except for Si, which remains primarily segregated at the original boundary position. This fact has not been reported before, and it indicates that the time at which the migrating boundary stays at each new position is not sufficient to build up a significant Si enrichment at the boundary, and therefore Si enrichment is only detected at the original boundary position. Grain boundary migration involving diffusion of solute atoms is known as diffusion-induced grain boundary migration (DIGM) [48]. The migration is induced by differences in chemical potential between the two grains on either side of the boundary and the boundary itself [49]. One of the proposed mechanisms is based on the climbing of grain boundary dislocations in response to a grain boundary Kirkendall effect [50,51]. Asymmetrical elemental profiles have been reported for in-reactor neutron irradiated bulk specimens of 20Cr–25Ni Nb-stabilised stainless steel [10,12,13] and also for TEM foils of the same steel grade irradiated in situ with 1 MeV electrons [11]. The asymmetry in elemental profiles is ascribed by Norris and co-worker to DIGM [13]. Additionally, radiation-induced grain boundary migration has been studied extensively in model Fe–⊜Cr–Ni alloys during in-situ electron irradiation [52–56]. These studies revealed an increase in Cr depletion due to the concomitant movement of the relevant grain boundary, and also ascribed the asymmetry in the measured profiles to the boundary migration during irradiation [52–56]. The boundary migration was proposed to be driven by the atomic rearrangement on the boundary interfacial plane via annihilation of point defects [52,54], which is in agreement with the dislocation climbing mechanism at the grain boundary mentioned above [57,58]. A model for RIS taking into account grain boundary migration has been proposed for

concentrated model alloys [59]. A term proportional to the velocity of the grain boundary movement was added to the diffusion equations, and the resultant model successfully simulated the asymmetrical experimental profiles observed in Fe–Cr–Ni alloys [59]. A comparison between the elemental profiles collected in the present study and those reported by Refs. [10–13] suggests that the comparatively larger extension of the boundary migration observed in this case may be to the proximity of the foil surface. However, the presence of significant radiation-induced defect fluxes and atomic rearrangement at the boundary seem to be a pre-requisite, since the annealing at those temperatures of reference thin TEM foils in the absence of proton irradiation did not reveal significant grain boundary migration.

DIGM has been reported previously only for HAGBs, and this fact agrees well with the experimental observations of this study. The observed migrating boundaries all have misorientation angles $\theta \geq 30°$ and the extent of the boundary migration, which is in this study is considered to be proportional to the width of the asymmetric elemental profile, depends on the misorientation angle, see Fig. 9. The grain boundaries where evidence of significant migration has been observed are those with θ>40°, with the only exception of a single boundary with $\theta = 33.6°$ at 500 °C. For these boundaries the profile width increases with the misorientation angle, until the misorientation angle characteristic of CSL Σ3 is reached. For boundaries with CSL Σ3 symmetry no significant elemental segregation/depletion has been observed.

Variations in the local elemental composition at dislocations lines were also detected, see Fig. 4, and they mirror the elemental profiles measured at grain boundaries. However, the magnitude and extension are reduced, potentially due to the minor sink strength of dislocation lines with respect to grain boundary [60], with the except of Si which segregates at a higher degree at dislocations than at grain boundaries. Radiation-induced elemental segregation at dislocations can induce the formation of second phases, if the solubility limit is exceeded locally. A radiation-induced nickel-silicide Ni_3Si, termed γ', has often been observed at dislocations in neutron-irradiated austenitic stainless steels [8,9,61–63], and Taylor reported this phase amongst those found in AGR cladding after in-reactor service, in those claddings irradiated between 369 °C and 480 °C for damage levels between 1 and 2 dpa [18]. However, we have not detected evidence of γ' precipitation in our study probably because the damage level we reached (0.8 dpa) is too low for the precipitation of this phase [61]. Moreover, the intermetallic phase known as G-phase has also been observed in AGR cladding after reactor service [18,62]. This second phase is thought to be induced by radiation in austenitic stainless steels [61]. However, in 20Cr–25Ni Nb-stabilised stainless steel G-phase was also observed in the microstructure after thermal ageing [64,65]. It was suggested that Nb(C,N) particles gradually evolve towards G-phase, releasing C and N into the surrounding austenitic matrix [64]. In the present study, G-phase was not found in the as-recrystallised material. However, significant Ni & Si segregation was detected at the Nb(C,N) particle/matrix interface after proton irradiation to 0.8 dpa at both 460 °C and 500 °C, see Fig. 5. This observation may support the hypothesis that Nb(C,N) particles evolve into G-phase, and proton irradiation would in this case accelerate this transformation.

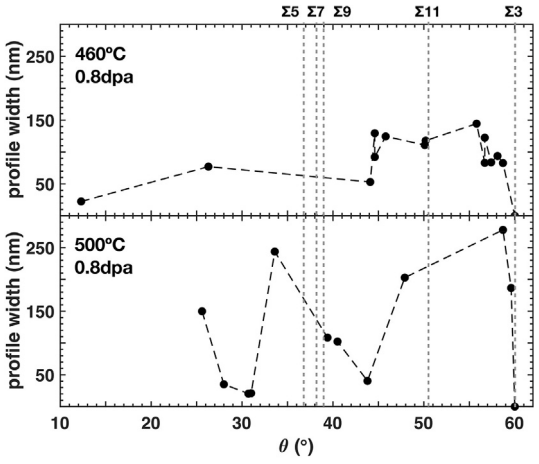

Fig. 9. Variation of the width of the Cr profile with the misorientation angle of the grain boundary at 460 °C and 500 °C. The grey vertical lines indicate the position of the special CLS boundaries Σ3, Σ5, Σ9 and Σ11.

A systematic study and reliable prediction of localised corrosion attacks during wet storage of the AGR steel cladding and spent fuel relies on the availability of sensitised cladding material for corrosion tests. In the past, thermal sensitisation has been used for the production of test specimens [66–68], however critical differences in the thermal-sensitised microstructure (absence of dislocation network, presence of second phases at grain boundaries and different width of the depleted zone) with respect to in-reactor irradiated specimens make the thermal-sensitisation route unsuitable. In this in-proton-irradiation study, we have used a dose rate of ~10^{-4} dpa/s, which is four orders of magnitude higher than the typical dose rate of an AGR reactor (~10^{-8} dpa/s [41]). Therefore, based on Mansur's equation for temperature shift to compensate for differences in dose rate [69], an increase from 420 °C, temperature at which peaked RIS and significant corrosion attacks have been observed in neutron-irradiated AGR cladding, to 500 °C for a proton irradiation with our dose rate, would lead to an equivalent damaged microstructure. The comparison between our proton-irradiated results and the limited data available regarding RIS in neutron-irradiated AGR cladding stainless steel [10–13,19,70] suggests that a proton irradiation temperature of 460 °C and a total damage of 0.8 dpa is sufficient to obtain a similar damaged microstructure and sensitisation to that observed in AGR cladding irradiated in reactor at 420 °C to a total damage of 2.2 dpa [22]. In both cases, double and asymmetrical profiles at grain boundaries with Cr content as low as 12 wt% have been detected [10,12,13]. The main difference detected in the RIS profiles between the in-reactor neutron irradiation specimens and the in-situ proton irradiated TEM foils of this study is the width of the Cr depleted regions, which is < 100 nm in the neutron irradiated samples, even for migrating boundaries [10,12,13]. This might be related to the fact that in our case the specimen was a thin TEM foil, where the boundaries were freer to migrate, increasing the width of the depleted zone. The importance of other surface effects depends on the target material and thickness, the irradiation temperature and the incident particles [71]. For foils ≥200 nm, microstructural evolutions comparable to bulk materials have been observed [71], whereas for intermediate thicknesses the surface sink strength for defects increases with irradiation temperature [72]. The samples used in the present study have a thickness ~110–140 nm, therefore it is expected that the lattice defect evolution is affected by the thickness [22]. However, the main characteristics of the RIS profiles, other than the profile width, seem to be not affected significantly by surface effects for the used irradiation conditions. The results of this work reveal that the severity of Cr depletion is higher in HAGBs, and that temperature effects under irradiation can induce boundary migration in AGR steel claddings and enhance the Cr depletion profile. Models accounting for the grain boundary internal structure and mobility, together with the competing effect of dislocation structures and second phase particles, are currently needed for AGR cladding stainless steel, in order to simulate RIS effects and

subsequently predict degradation of those claddings during wet storage. Modelling efforts in this direction have been reported for other stainless steel grades and for irradiation conditions relevant for Light Water Reactors [15,16,59]. However, a coherent modelling work based on the reported experimental evidence is still needed for AGR cladding material.

5. Conclusions

We have performed an in-depth characterisation of the local solute redistribution at defects sinks in 20Cr–25Ni austenitic stainless steel induced by proton irradiation, for a damage level of 0.5 dpa at 420 °C and 0.8 dpa at 460 °C and 500 °C. The main results of this study are:

- Depletion of Cr, Fe and Mn and segregation of Ni and Si have been observed at all the irradiation temperatures at grain boundaries, radiation-induced dislocations and second phase particles. The intensity and the width of the local chemical depletion/segregation increases with temperature up to 500 °C.
- At all temperatures investigated, we have observed a dependence of the measured elemental profiles with the grain boundary character, and for misorientation angles approaching 60° there is a decrease of the Cr depletion. Highly coherent grain boundaries, such as CSL Σ3, would therefore be RIS-resistant.
- Grain boundary migration at 460 °C, and especially noticeable at 500 °C, strongly affects the elemental profiles across grain boundaries, giving rise to asymmetrical and broadened profiles, with the Cr content reaching its minimum values.
- Ni and Si clustering has been observed close to radiation-induced dislocations. However, no γ' precipitation has been detected at those locations. In contrast, the Ni and Si segregation at the Nb(C,N)/matrix interface leads to the formation of a shell-like structure, and may hint to a radiation-enhanced transition of Nb(C,N) particles into G-phase.

These results open the door (i) to simulate systematically neutron-induced sensitisation of AGR steel claddings using intense proton beams, and also (ii) to enhance the existing models about radiation-induced sensitisation in austenitic stainless steels by adding structural and mobility information about grain boundaries, together with the competing effects of dislocations and second phase particles for diffusing point defects and solute atoms.

Acknowledgments

We acknowledge the Engineering and Physical Sciences Research Council for providing funding for this project (EP/L014041/1), and for the development of the MIAMI-2 Facility (EP/M028283/1) and access via the UK National Ion Beam Centre. We would also like to thank Dr. S. Walters from the National Nuclear Laboratory for providing the starting material.

Appendix A. Supplementary data

Supplementary data to this article can be found online at https://doi.org/10.1016/j.jnucmat.2019.02.035.

References

[1] V. Ramaswamy, D.R.F. West, NbC Precipitation in 20%Cr-25%Ni-1%Nb Austenitic Steel, J. Iron Steel Inst. 208 (1970) 391–394.
[2] C. Barcellini, S. Dumbill, E. Jimenez-Melero, Isothermal annealing behaviour of nuclear grade 20Cr-25Ni austenitic stainless steel, Mater. Char. 145 (2018) 303–311, https://doi.org/10.1016/J.MATCHAR.2018.08.057.
[3] G. Knowles, The Creep Strength of 20%Cr-25%Ni-Nb Steel Containing Controlled Particle Dispersions, Met. Sci. (1977) 117–122.
[4] T. Sourmail, Precipitation in creep resistant austenitic stainless steel, Mater. Sci. Technol. 17 (2001).
[5] NDA Corporate report, Oxide Fuels Preferred Option, 2012. SMS/TS/C2-OF/001.
[6] D. Pearce, L. Edwards, G. Beuret, The Windscale Inquiry: the Proceedings, in: Decis. Mak. Energy Futur. A Case Study Wind. Inq., Palgrave Macmillan UK, London, 1979, pp. 130–183, https://doi.org/10.1007/978-1-349-04985-1_7.
[7] G.S. Was, Fundamentals of Radiation Materials Science: Metals and Alloys, Springer, 2007.
[8] S.M. Bruemmer, E.P. Simonen, P.M. Scott, P.L. Andresen, G.S. Was, J.L. Nelson, Radiation-induced material changes and susceptibility to intergranular failure of light-water-reactor core internals, J. Nucl. Mater. 274 (1999) 299–314, https://doi.org/10.1016/S0022-3115(99)00075-6.
[9] G.S. Was, T.R. Allen, J.T. Busby, J. Gan, D. Damcott, D. Carter, M. Atzmon, E.A. Kenik, Microchemistry and microstructure of proton-irradiated austenitic alloys: toward an understanding of irradiation effects in LWR core components, J. Nucl. Mater. 270 (1999) 96–114, https://doi.org/10.1016/S0022-3115(98)00897-6.
[10] C. Taylor, The Formation of Sensitised Microstructures during the Irradiation of CAGR Fuel Pin Cladding, in: D.I.R. Norris (Ed.), Radiation-Induced Sensitisation Stainl. Steel, Berkeley Nuclear Laboratories, 1986.
[11] M.A. Ashworth, D.I.R. Norris, I.P. Jones, Radiation-Induced Segregation in Fe/20Cr/25Ni/Nb Based Austenitic Stainless Steel, J. Nucl. Mater. 189 (1992) 289–302.
[12] D.I.R. Norris, C. Baker, J.M. Titchmarsh, Compositionl Profiles at Grain Boundaries in 20%Cr/25%Ni/Nb Steinless Steel, in: D.I.R. Norris (Ed.), Radiation-Induced Sensitisation Stainl. Steel, Berkeley Nuclear Laboratories, 1987, p. 87.
[13] D.I.R. Norris, C. Baker, C. Taylor, J.M. Titchmarsh, Radiation-Induced Segregation in 20Cr/25Ni/Nb Stainless Steel, vol. 1125, ASTM STP, 1992.
[14] K.G. Field, L.M. Barnard, C.M. Parish, J.T. Busby, D. Morgan, T.R. Allen, Dependence on grain boundary structure of radiation induced segregation in a 9 wt.% Cr model ferritic/martensitic steel, J. Nucl. Mater. 435 (2013) 172–180, https://doi.org/10.1016/J.JNUCMAT.2012.12.026.
[15] T.S. Duh, J.J. Kai, F.R. Chen, L.H. Wang, Numerical simulation modeling on the effects of grain boundary misorientation on radiation-induced solute segregation in 304 austenitic stainless steels, J. Nucl. Mater. 294 (2001) 267–273.
[16] T.S. Duh, J.J. Kai, F.R. Chen, Effects of grain boundary misorientation on solute segregation in thermally sensitized and proton-irradiated 304 stainless steel, J. Nucl. Mater. 283–287 (2000) 198–204, https://doi.org/10.1016/S0022-3115(00)00255-5.
[17] S. Watanabe, Y. Takamatsu, N. Sakaguchi, H. Takahashi, Sink effect of grain boundary on radiation-induced segregation in austenitic stainless steel, J. Nucl. Mater. 283–287 (2000) 152–156, https://doi.org/10.1016/S0022-3115(00)00204-X.
[18] C. Taylor, Precipitation in 20 Cr-25 Ni type stainless steel irradiated at low temperatures in a thermal reactor (AGR), in: Dimens. Stab. Mech. Behav. Irradiat. Met. Alloy, 1983, pp. 47–50, https://doi.org/10.1680/dsamboimaav1.01756.0012.
[19] D.I.R. Norris, C. Baker, J.M. Titchmarsh, A study of radiation-induced sensitusation in 20/25/Nb steel by compositional profile measurements at grain boundaries, in: B.N.E. Society (Ed.), Mater. Nucl. React. Core Appl, 1987.
[20] J.A. Hinks, A review of transmission electron microscopes with in situ ion irradiation, Nucl. Instrum. Methods Phys. Res. Sect. B Beam Interact. Mater. Atoms 267 (2009) 3652–3662, https://doi.org/10.1016/J.NIMB.2009.09.014.
[21] S. Ishino, A review of in situ observation of defect production with energetic heavy ions, J. Nucl. Mater. 251 (1997) 225–236, https://doi.org/10.1016/S0022-3115(97)00247-X.
[22] C. Barcellini, R.W. Harrison, S. Dumbill, S.E. Donnelly, E. Jimenez-Melero, Evolution of radiation-induced lattice defects in 20/25 Nb-stabilised austenitic stainless steel during in-situ proton irradiation, J. Nucl. Mater. 514 (2019) 90–100, https://doi.org/10.1016/J.JNUCMAT.2018.11.019.
[23] G.S. Was, J.T. Busby, T. Allen, E.A. Kenik, A. Jensson, S.M. Bruemmer, J. Gan, A.D. Edwards, P.M. Scott, P.L. Andreson, Emulation of neutron irradiation effects with protons: validation of principle, J. Nucl. Mater. 300 (2002) 198–216. https://doi.org/10.1016/S0022-3115(01)00751-6.
[24] J. Gan, G.S. Was, Microstructure evolution in austenitic Fe–Cr–Ni alloys irradiated with protons: comparison with neutron-irradiated microstructures, J. Nucl. Mater. 297 (2001) 161–175, https://doi.org/10.1016/S0022-3115(01)00615-8.
[25] F. Bachmann, R. Hielscher, H. Schaeben, Texture Analysis with MTEX – Free and Open Source Software Toolbox, in: Texture Anisotropy Polycrystals III, Trans Tech Publications, 2010, pp. 63–68.
[26] F.J. Humphreys, Review Grain and subgrain characterisation by electron backscatter diffraction, J. Mater. Sci. 36 (2001) 3833–3854. https://doi.org/10.1023/A:1017973432592.
[27] F.J. Humphreys, Quantitative metallography by electron backscattered diffraction, J. Microsc. 195 (1999) 170–185. https://doi.org/10.1046/j.1365-2818.1999.00578.x.
[28] M.L. Kronberg, F.H. Wilson, Secondary recrystallization in copper, MetalsTransactions 185 (1949) 501–514. https://doi.org/10.1007/BF03398387.
[29] V. Randle, A. Brown, Development of grain misorientation texture, in terms of coincident site lattice structures, as a function of thermomechanical treatments, Philos. Mag. A 59 (1989) 1075–1089, https://doi.org/10.1080/

01418618908209838.
[30] D.G. Brandon, The structure of high-angle grain boundaries, Acta Metall. 14 (1966) 1479–1484. http://www.sciencedirect.com/science/article/pii/0001616066901684.
[31] D. Delille, R. Pantel, E. Van Cappellen, Crystal thickness and extinction distance determination using energy filtered {CBED} pattern intensity measurement and dynamical diffraction theory fitting, Ultramicroscopy 87 (2001) 5–18. https://doi.org/10.1016/S0304-3991(00)00067-X.
[32] R.E. Stoller, M.B. Toloczko, G.S. Was, A.G. Certain, S. Dwaraknath, F.A. Garner, On the use of {SRIM} for computing radiation damage exposure, Nucl. Instrum. Methods Phys. Res. Sect. B Beam Interact. Mater. Atoms 310 (2013) 75–80. https://doi.org/10.1016/j.nimb.2013.05.008.
[33] Y. Zhang, https://www.fei.com/products/tem/talos-f200x-for-materials-science/, (n.d.).
[34] D.B. Williams, C.B. Carter, Transmission Electron Microscopy: A Textbook for Materials Science, Springer, 2009.
[35] R.R. Keller, R.H. Geiss, Transmission EBSD from 10 nm domains in a scanning electron microscope, J. Microsc. 245 (2011) 245–251, https://doi.org/10.1111/j.1365-2818.2011.03566.x.
[36] G.C. Sneddon, P.W. Trimby, J.M. Cairney, Transmission Kikuchi diffraction in a scanning electron microscope: A review, Mater. Sci. Eng. R Rep. 110 (2016) 1–12, https://doi.org/10.1016/J.MSER.2016.10.001.
[37] A.D. Marwick, Segregation in irradiated alloys: The inverse Kirkendall effect and the effect of constitution on void swelling, J. Phys. F Met. Phys. 8 (1978) 1849. http://stacks.iop.org/0305-4608/8/i=9/a=008.
[38] H. Wiedersich, P.R. Okamoto, N.Q. Lam, A theory of radiation-induced segregation in concentrated alloys, J. Nucl. Mater. 83 (1979) 98–108. https://doi.org/10.1016/0022-3115(79)90596-8.
[39] S. Watanabe, H. Takahashi, Discriminant of RIS in multi-component alloys, J. Nucl. Mater. 208 (1994) 191–194, https://doi.org/10.1016/0022-3115(94)90211-9.
[40] S.J. Rothman, L.J. Nowicki, G.E. Murch, Self-diffusion in austenitic Fe-Cr-Ni alloys, J. Phys. F Met. Phys. 10 (1980) 383–398, https://doi.org/10.1088/0305-4608/10/3/009.
[41] J.M. Perks, A.D. Marwick, C.A. English, A computer code to calculate the radiation-indiced segregation in concentrated ternary alloys, Harwell, Oxfordshire OX11 0RAn, 1986.
[42] J.M. Perks, A.D. Marwick, C.A. English, Fundamental Aspects of radiation-induced Segregation in Fe-Cr-Ni Alloys, in: D.I.R. Norris (Ed.), Radiation-Induced Sensitisation Stainl. Steel, Berkeley Nuclear Laboratories, 1986.
[43] D.L. Damcott, T.R. Allen, G.S. Was, Dependence of radiation-induced segregation on dose, temperature and alloy composition in austenitic alloys, J. Nucl. Mater. 225 (1995) 97–107, https://doi.org/10.1016/0022-3115(94)00690-3.
[44] A. Kavner, T.M. Devine, Effect of grain boundary orientation on the sensitization of austenitic stainless steel, J. Mater. Sci. 32 (1997) 1555–1562, https://doi.org/10.1023/A:1018530723348.
[45] M.S. Laws, P.J. Goodhew, Grain boundary structure and chromium segregation in a 316 stainless steel, Acta Metall. Mater. 39 (1991) 1525–1533, https://doi.org/10.1016/0956-7151(91)90238-V.
[46] T. Watanabe, Structural effects on grain boundary segregation, hardening and fracture, J. Phys. Colloq. 46 (1985). C4-555-C4-566.
[47] R. Jones, V. Randle, Sensitisation behaviour of grain boundary engineered austenitic stainless steel, Mater. Sci. Eng. 527 (2010) 4275–4280. https://doi.org/10.1016/j.msea.2010.03.058.
[48] A.H. King, Diffusion induced grain boundary migration, Int. Mater. Rev. 32 (1987) 173–189, https://doi.org/10.1179/095066087790150304.
[49] M. Hillert, On the driving force for diffusion induced grain boundary migration, Scripta Metall. 17 (1983) 237–240, https://doi.org/10.1016/0036-9748(83)90105-9.
[50] R.W. Balluffi, J.W. Cahn, Mechanism for diffusion induced grain boundary migration, Acta Metall. 29 (1981) 493–500, https://doi.org/10.1016/0001-6160(81)90073-0.
[51] D.A. Smith, A.H. King, On the mechanism of diffusion-induced boundary migration, Philos. Mag. A 44 (1981) 333–340, https://doi.org/10.1080/01418618108239536.
[52] H. Takahashi, N. Hashimoto, Radiation-Induced Segregation and Grain Boundary Migration in Fe–Cr–Ni Model Alloy under Irradiation, Mater. Trans. 34 (1993) 1027–1030. https://doi.org/10.2320/matertrans1989.34.1027.
[53] H. Takahashi, N. Hashimoto, S. Watanabe, Defect-flow-induced grain boundary migration with segregation under electron irradiation, Ultramicroscopy 56 (1994) 193–197.
[54] S. Watanabe, N. Sakaguchi, N. Hashimoto, H. Takahashi, Quantitative studies of irradiation-induced segregation and grain boundary migration in FeCrNi alloy, J. Nucl. Mater. 224 (1995), 158. 8.
[55] S. Watanabe, N. Sakaguchi, N. Hashimoto, M. Nakamura, H. Takahashi, C. Namba, N.Q. Lam, Radiation-induced segregation accompanied by grain boundary migration in austenitic stainless steel, J. Nucl. Mater. 232 (1996) 133.
[56] N. Sakaguchi, N. Shibayama, T. Kinoshita, H. Takahashi, H, Atomistic observation of radiation-induced grain-boundary movement in Fe-Cr-Ni alloy under electron irradiation, Phil. Mag. Lett. 81 (2001) 691–696.
[57] A.H. King, D.A. Smith, On the mechanisms of point-defect absorption by grain and twin boundaries, Phil. Mag. 42 (1980) 495–512. https://doi.org/10.1080/01418618008239372.
[58] A.H. King, D.A. Smith, The effects on grain-boundary processes of the steps in the boundary plane associated with the cores of grain-boundary dislocations, Acta Crystallogr. A (1980) 335–343. https://doi:10.1107/S0567739480000782.
[59] N. Sakaguchi, S. Watanabe, H. Takahashi, A new model for radiation-induced grain boundary segregation with grain boundary movement in concentrated alloy system, J. Mater. Sci. 40 (2005) 889–893.
[60] Z. Jiao, G.S. Was, Novel features of radiation-induced segregation and radiation-induced precipitation in austenitic stainless steels, Acta Mater. 59 (2011) 1220–1238, https://doi.org/10.1016/J.ACTAMAT.2010.10.055.
[61] K. Russell, Phase stability under irradiation, Prog. Mater. Sci. 28 (1984) 229–434, https://doi.org/10.1016/0079-6425(84)90001-X.
[62] T.M. Williams, J.M. Titchmarsh, D.R. Arkell, A nickel-and silicon-rich phase in irradiated FV548 steel, J. Nucl. Mater. 82 (1979) 199–201. https://doi.org/10.1016/0022-3115(79)90055-2.
[63] C.F. Bilsby, V.B. Livesey, F.W. Morris, M. Turek, Observation of G phase in Advanced Gas-cooled Reactor (AGR) 20/25Nb stabilised stainless steel end caps, 1983.
[64] D.J. Powell, R. Pilkington, D.A. Miller, The Precipitation Characteristics of 20% Cr/25%Ni - Nb Stabilised Stainless Steel, Acta 36 (1988).
[65] R.C. Ecob, R.C. Lobb, V.L. Kohler, The Formation of G-phase in 20/25 Nb Stainless Steel AGR Fuel Cladding Alloy and its Effect on Creep Properties, J. Mater. Sci. 22 (1987) 2867–2880.
[66] G.O.H. Whillock, B.J. Hands, T.P. Majchrowski, D.I. Hambley, Investigation of thermally sensitised stainless steels as analogues for spent AGR fuel cladding to test a corrosion inhibitor for intergranular stress corrosion cracking, J. Nucl. Mater. 480 (2018) 187–198.
[67] A. Al-Shater, D. Engelberg, S. Lyon, C. Donohoe, S. Walters, G. Whillock, A. Sherry, Characterization of the stress corrosion cracking behavior of thermally sensitized 20Cr-25Ni stainless steel in a simulated cooling pond environment, J. Nucl. Sci. Technol. 54 (2017) 742–751.
[68] C.J. Moss, J.M. Sykes, Thermal Sensitisation of 20Cr/25Ni/Nb Stainless Steel, in: D.I.R. Norris (Ed.), Radiation-Induced Sensitisation Stainl. Steel, Berkeley Nuclear Laboratories, 1986.
[69] L.K. Mansur, Theory of transitions in dose dependence of radiation effects in structural alloys, J. Nucl. Mater. 206 (1993) 306–323. https://doi.org/10.1016/0022-3115(93)90130-Q.
[70] J.M. Titchmarsh, I.A. Vatter, Measurement of radiation-induced segregation profiles by high spatial resolution electron microscopy, in: D.I.R. Norris (Ed.), Radiation-induced Sensitisation Stainl. Steel, Berkeley Nuclear Laboratories, 1986.
[71] S. Ishino, A review of in situ observation of defect production with energetic heavy ions, J. Nucl. Mater. 251 (1997) 225–236.
[72] S. Ishino, K. Fukuya, T. Muroga, N. Sekimura, H. Kawanishi, In-situ microstructural observation of radiation damage in nickel produced by energetic heavy particles, J. Nucl. Mater. 122 (1984) 597–601.